

## Article

# Performance Analysis on the Small-Scale Reusable Launch Vehicle

Zheng Gong <sup>1</sup>, Zian Wang <sup>2,\*</sup> , Chengchuan Yang <sup>1</sup>, Zhengxue Li <sup>2</sup>, Mingzhe Dai <sup>3</sup>  and Chengxi Zhang <sup>4</sup> 

<sup>1</sup> Department of Aerospace Engineering, Nanjing University of Aeronautics and Astronautics, Nanjing 210016, China

<sup>2</sup> China Academy of Launch Vehicle Technology, Beijing 100076, China

<sup>3</sup> School of Automation, Central South University, Changsha 410083, China

<sup>4</sup> School of Electronic and Information Engineering, Harbin Institute of Technology, Harbin 150006, China

\* Correspondence: wangzian@nuaa.edu.cn

**Abstract:** According to the symmetrical characteristics of a new type of Reusable Launch Vehicle (RLV) in the recovery phase, we studied the basic aerodynamic model data of Starship and the aerodynamic data with rudder deflection, and the causes of its aerodynamic coefficients are expounded. At the same time, we analyzed its stability and maneuverability. According to the flying quality requirements, the lateral-directional model of Starship in the return phase at a high angle of attack is analyzed. Finally, we analyzed the lateral heading stability and control deviation of Starship by using the criterion and nonlinear open-loop simulations. The results show that the Starship has pitching and rolling stability, but it only has heading stability in some ranges of angle of attack, and there is no heading stability at a conventional large angle of attack. At the same time, after modal analysis and comparison of flight quality, it can be seen that the longitudinal long-period model of the starship degenerates into a real root and it is stable and convergent. The lateral heading roll mode is at level 2 flight quality, the helical mode is at level 1 flight quality, and the Dutch roll mode diverges, which needs to be stabilized and controlled later.

**Keywords:** Reusable Launch Vehicle; stability; manipulateness; flying qualities; criterion analysis



**Citation:** Gong, Z.; Wang, Z.; Yang, C.; Li, Z.; Dai, M.; Zhang, C. Performance Analysis on the Small-Scale Reusable Launch Vehicle. *Symmetry* **2022**, *14*, 1862. <https://doi.org/10.3390/sym14091862>

Academic Editors: Jan Awrejcewicz and Sergei D. Odintsov

Received: 9 July 2022

Accepted: 30 August 2022

Published: 6 September 2022

**Publisher's Note:** MDPI stays neutral with regard to jurisdictional claims in published maps and institutional affiliations.



**Copyright:** © 2022 by the authors. Licensee MDPI, Basel, Switzerland. This article is an open access article distributed under the terms and conditions of the Creative Commons Attribution (CC BY) license (<https://creativecommons.org/licenses/by/4.0/>).

## 1. Introduction

Since the former Soviet Union cosmonaut Gagarin [1] entered space for the first time, after more than 60 years of continuous exploration and development in the field of manned space flight, so far, there are two types of manned spacecraft in the world that can carry out missions between space and earth: the space shuttle of the United States [2] and manned spacecraft represented by Soyuz of Russia and Shenzhou of China [3,4]. However, except for a small part of the space shuttle, other manned spacecraft are not reusable, and the maintenance cost of space shuttles is very expensive, so the cost of space travel has been exceedingly high, which greatly restricts the pace of human exploration of outer space.

Starship and Super Heavy are the next generation of reusable space transportation systems proposed by Musk, founder of SpaceX, based on the vision of Mars colonization. According to the company's assumption, a wide range of missions can be accomplished through a variety of combinations of the two core spacecraft: interplanetary missions such as manned landing on Mars, near-earth missions such as space station transportation, satellite deployment, and globally ultra-fast passenger transportation. A recent lunar version of the starship program also won NASA's bid for the Moon landing mission. As a result, this system can theoretically meet the requirements of large-span transportation activities between different spaces, ranging from near-earth activities to Mars colonization.

In recent years, with the development of civil aerospace enterprises, new opportunities and challenges have been brought to the aerospace field. Since SpaceX publicized the ITS program in 2016, the Starship program has undergone several major design changes and

evolutions. In 2019, the first starship prototype was publicly displayed. Since then, SpaceX has accelerated the research and manufacturing of starships by adopting the strategy of rapid testing and iterative verification of prototypes: In 2019, the free suspension test and safe landing test of the star worm preliminary verifier were completed [5]. Since 2020, through intensive flight tests of prototypes SN5–SN15 [6–10], SpaceX gradually mastered the key technologies of suspension at a low altitude of 150 m, flight at a high altitude of 10 km, roll maneuver, engine restarting powered braking, vertically soft landing at a fixed point, and so on [11–15]. According to the current progress, the orbital flight test of the Starship–Super Heavy system with high integration and comprehensive assessment is expected to be realized soon, and the system is planned to be used for carrying out manned missions such as landing on the Moon and Mars in the future [16–18].

The Starship–Super Heavy transportation system uses a two-stage fully reusable vehicle scheme with a designed loading capacity of 100 t. After the superheavy booster completes the first-stage powered flight separation, the starship continues the second-stage powered flight and continues to accelerate to enter orbit. The design of the starship is a combination of a two-stage rocket, orbiter, and reentry vehicle. The crew and payload are placed in the load cabin at the front of the starship, which has a reentry and return capability similar to that of the space shuttle orbiter [18–20]. The starship can carry a 50 t payload on return and uses a power-braking vertical fixed-point recovery scheme during the landing phase, which is similar to the Falcon 9 rocket [21,22]. With a simple shape and body of cone-column combination, the starship adopts a unique tailless canard aerodynamic configuration, and in order to meet the requirements of reentry flight, thermal tiles are laid on the windward side to deal with the thermal environment during reentry flight [23]. The current aerodynamic layout scheme of the starship is different not only from the manned spacecraft and space shuttle schemes of the traditional space transportation system, but also from the radical air-space shuttle scheme, and it is even significantly different from the earlier scheme, thus attracting huge attention once proposed [24,25]. Different from both the conventional manned spacecraft that is recovered by parachutes after semi-ballistic reentry into the atmosphere, and the space shuttle that lands horizontally on the airport, the landing method that the starship adopts is more similar to the recovery landing method of the rocket “Falcon”, which realizes the vertical landing by the coordinated control of rudder surfaces and vector thrust. A new rudder surface control that is different from the traditional lift-body aircraft is adopted in the starship for this special takeoff and landing way [26]. Traditional lift-body aircraft realize the control of attitude and path by adopting the ailerons and vertical and horizontal tails, while the starship controls its body through two pairs of wings scattered on the nose and tail, which can deflect along the axial direction [27]. Zuo [27] made a detailed analysis of aerodynamic characteristics of the shape of the early starships (2019) in the landing and low-speed stages. Combined with aerodynamic characteristics such as lift/drag obtained from the simulation of subsonic separation flow field under a large angle of attack and the changing rules of the vertex moment along the deflection angle of leading and rear wings, a conclusion that four wings of the starship layout are subject to the three-channel control was given. While during the hypersonic and supersonic flight of reentry process, how about the wide speed-domain characteristics of this configuration, whether reentry trimming at full speed domain can be realized, how about the characteristics of the center of mass, whether the three channels are stable, what outstanding characteristics and advantages this configuration have, why such a unique design is taken, and many other problems remain to be further analyzed and researched.

At present, domestic and foreign studies on manipulateness stability characteristics analysis are only limited to aircraft or taxiway takeoff and landing vehicles, and the structure is relatively simple, such as studies on multivariable stability margin of reentry aircraft [28], definitions of static stability margin of aircraft [29], and state feedback control and stability analysis of hypersonic aircraft [30]. There is also research on modal stability analysis of hypersonic aircraft with lift-body configuration [31], aerodynamic characteristics

analysis of X-33-like vehicles [32], longitudinal and lateral flight quality research of saucer aircraft [26,27], flight quality research of short take-off and vertical landing aircraft, criterion analysis of Robert Weissman, etc. However, there is little research on the manipulateness and stability characteristics and flight quality of RLVs that can take off and land vertically.

This paper focuses on the starships, in view of the large angle of attack flight characteristics during the recovery phase. The stability characteristics of aerodynamic derivatives are analyzed, classical theory of flight dynamics of linearized small perturbation method is applied to work out the motion characteristic root of longitudinal and lateral direction, and analysis is carried out. At the same time, the principle of criteria is used to analyze the lateral-directional stability and control the deviation of the starship. Finally, time-history open-loop simulation is used to verify the above analysis.

## 2. Aerodynamic Configuration of Starships

This paper models the starship according to the size parameters publicized on the official website of SpaceX, as shown in Figure 1. The wings are arranged according to the canard layout, a pair of front wings are arranged at the cone section, and a pair of rear wings are arranged at the end of the column section, both of which adopt trapezoidal wings. The whole ship is 50 m in length, 9 m in diameter, about 18 m in rear wingspan, and 15 m in front wingspan. The projected area of the whole plane is about 545 square meters. The weight of the whole ship is  $10^5$  kg, and the fuselage is made of stainless steel. In light of the shape and the distribution of the inner fuel tank and engine, the center of gravity of the whole ship is estimated at 40 m from the nose, and the pitching axial inertia moment coming through the center of gravity is  $3.7 \times 10^7$  kg·m<sup>2</sup>.



**Figure 1.** Configuration of Starship.

Overall, as a lift reentry vehicle, its simple shape gives itself distinctive characteristics, but it also brings several questions.

The simple and coordinated shape of the cone-column -wing, which is facially symmetrical, intuitively facilitates the series combination with superheavy boosters with the same diameter to form a simple two-stage rocket configuration, and this is much more compact than the complicated parallel layout of the orbiter-fuel tank-booster of the space shuttle, and the corresponding aerodynamic characteristics, flight control, and design of booster separation during the active period are also much simpler. Is this simple configuration suitable for lift reentry and return flight in a superwide speed domain?

A canard layout with a front-rear wings combination is adopted. The canard layout is common in the design of tactical missiles and highly maneuverable fighters, but there is no precedent in the design of reentry vehicles. The canard layout with relaxed static stability technology can realize that all wings generate positive lift at the trimming state and improve the aerodynamic efficiency of the aircraft. However, is it necessary for the returning stage? In addition, the canard is located very near the front, which means that the starship may face a severe aerodynamic heating environment during supersonic flight, and will it cause a serious problem for thermal protection?

It is a significant change in comparison to the earlier starship schemes (both the September 2018 and December 2018 versions had vertical tails) that the new version adopts a tailless layout without vertical tails and ventral fin. Tailless design and canard configuration will lead to the directional pressure center moving forward significantly. Intuitively, it can be judged that the starship's directional pressure center will be too forward in most ranges of flight velocity and angle of attack. Will this pose a serious risk to the lateral-directional static stability?

### 3. Performance Analysis

The new small-scale RLV starship that can vertically take off and land has a wing-body fusion design with four new rudder surfaces (hereinafter referred to as "elevator-like", "aileron-like", and "rudder-like") at the front and rear for attitude motion. In order to evaluate its stability and maneuverability, it is necessary to analyze its manipulateness and stability characteristics. Figure 2 shows the scaling model obtained by modeling the shape layout published by SpaceX. The basic aerodynamic data and corresponding aerodynamic derivatives were obtained by Computational Fluid Dynamics (CFD) calculation of the layout, and the following analysis was made.

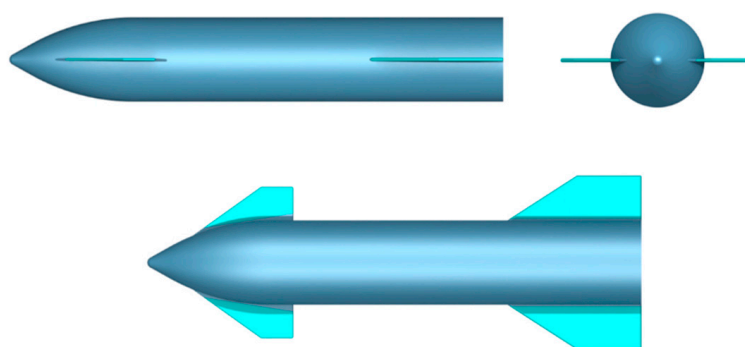


**Figure 2.** Configuration of small-scale Starship.

#### 3.1. Analysis of Static Force and Moment Coefficients

##### 3.1.1. Analysis of Polar Curve and Lift-Drag Ratio

In the absence of roll, yaw, and pitch, the changes of pole curve and lift-drag ratio with angle of attack are analyzed. The results are shown in Figures 3 and 4. The tangent line of the polar curve is drawn from the origin of the coordinate, the lift-drag ratio achieves its maximum at the tangent point, and the corresponding angle of attack is the favorable angle of attack  $\alpha_{opt}$ , which is  $20^\circ$ .

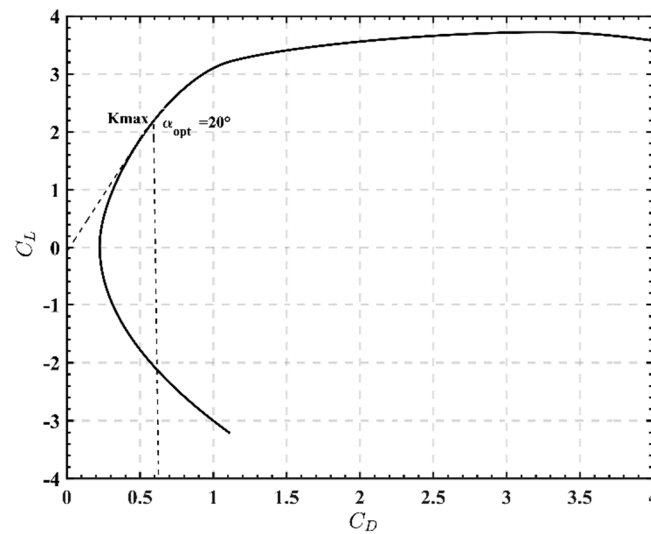


Figure 3. Polar curve.

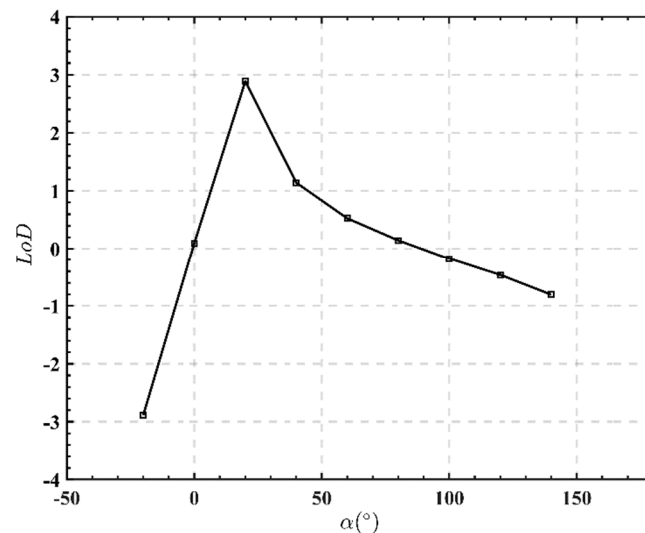


Figure 4. Lift–drag ratio.

### 3.1.2. Analysis of Longitudinal Forces and Moments

Keep the elevator-like, aileron-like, and rudder-like still,  $\delta_e = \delta_a = \delta_r = 0$ , and the rate of roll, pitch, and yaw angle is 0, namely, under the condition of  $p = q = r = 0$ , the starship's lift coefficient, drag coefficient, and roll moment coefficient curve is shown in Figures 5–7. In the figures,  $C_L$ ,  $C_D$ , and  $C_m$  are, respectively, lift coefficient, drag coefficient, and roll moment coefficient, and  $\alpha$  is angle of attack. It can be seen from the figures:

- (1) The lift coefficient increases with the increase in the angle of attack when  $-20^\circ < \alpha < 40^\circ$ , and decreases with the increase in the angle of attack when  $\alpha > 40^\circ$ .  $\alpha = 40^\circ$  is the critical angle of attack.
- (2) When  $0^\circ < \alpha < 80^\circ$ , the drag coefficient increases with the increase in the angle of attack; at  $-20^\circ < \alpha < 0^\circ$  and  $\alpha > 80^\circ$ , the drag coefficient decreases with the increase in the angle of attack. When the angle of attack is 0, the drag coefficient is the minimum; when the angle of attack is  $80^\circ$ , the drag coefficient is the maximum. So when the starship returns, choose a horizontal descent to minimize the speed of descent with maximum resistance.
- (3) When  $-20^\circ < \alpha < 0^\circ$ ,  $C_m > 0$ , a positive pitching moment is generated to make the starship raise its nose to reduce the angle of attack. Within the range of angle of attack

$\alpha > 0^\circ$ ,  $C_m < 0$ , a negative pitching moment is generated to make the starship bow its nose to reduce the angle of attack.

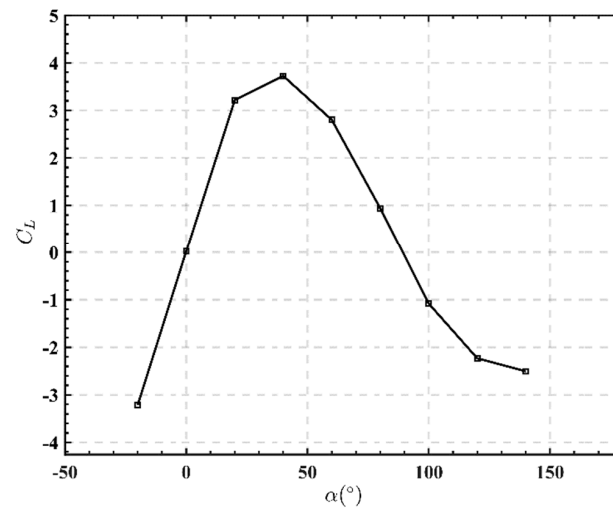


Figure 5. Lift coefficient.

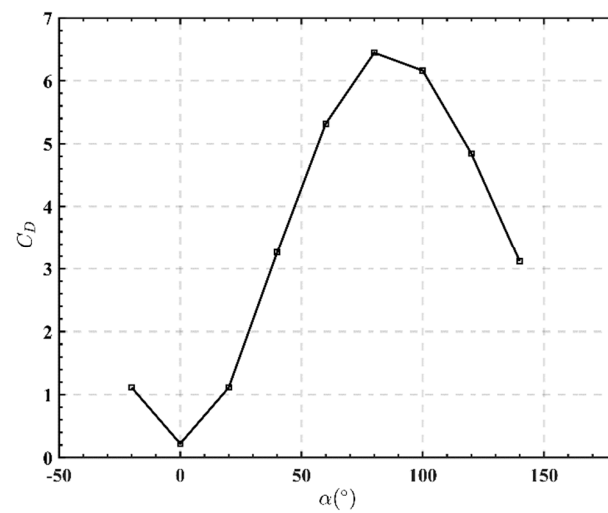


Figure 6. Drag coefficient.

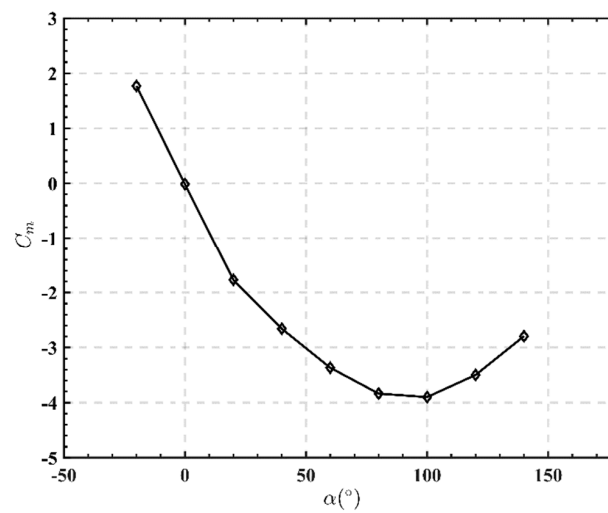


Figure 7. Pitch moment coefficient.

The above analysis shows that the changing rules of longitudinal static force and moment coefficient along the angle of attack are consistent with actual flight characteristics.

### 3.1.3. Lateral-Directional Force and Moment Analysis

Curves of the starship's lateral force coefficient, roll moment coefficient, and yaw moment coefficient are shown in Figures 8–10. In the figures,  $C_s$ ,  $C_l$ , and  $C_n$  are, respectively, the lateral force coefficient, roll moment coefficient, and yaw moment coefficient. It can be seen from the figures:

- (1) The variation of static lateral force coefficient with angle of attack is as follows: negative lateral force is generated if the side slip is positive, while if negative sideslip occurs, positive lateral force occurs.
- (2) When the positive side slip occurs, negative side force is generated, and then negative roll moment is generated, so the roll moment coefficient is negative; when negative sideslipping occurs, positive sideslipping force is generated, and then positive rolling moment is generated, so the rolling moment coefficient is positive.
- (3) When positive sideslip occurs, yaw moment coefficient is positive; when negative sideslip occurs, yaw moment coefficient is negative.

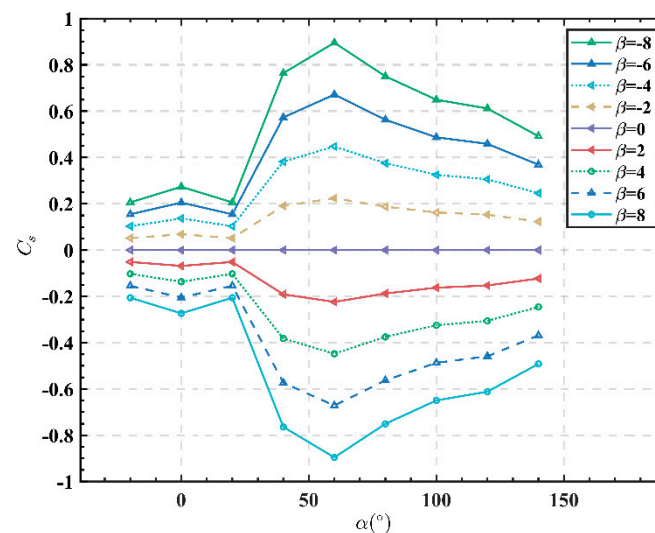


Figure 8. Lateral force coefficient.

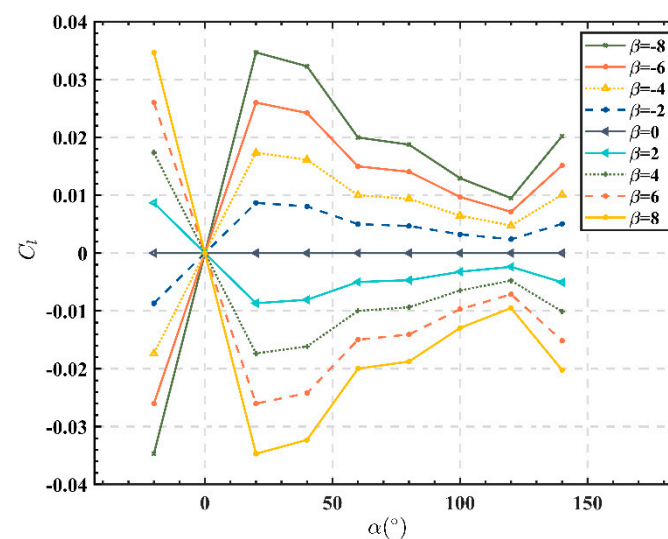


Figure 9. Roll torque coefficient.

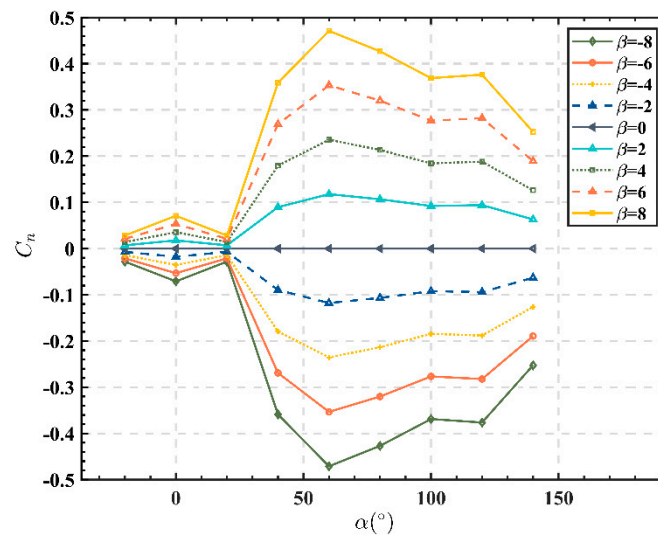


Figure 10. Yaw moment coefficient.

The above analysis shows that the lateral-directional static force and moment coefficient vary with the angle of attack in accordance with the actual flight characteristics.

### 3.1.4. Static Stability Analysis

The pitch static stability coefficient curve, roll static stability coefficient curve, and yaw static stability coefficient curve are shown in Figures 11–13. In the figures,  $C_{m\alpha}$  is the roll static stability coefficient,  $C_{l\beta}$  is the roll static stability coefficient, and  $C_{n\beta}$  is the yaw static stability coefficient. It can be seen from the figure that the pitching static stability of the starship decreases with the increase in the angle of attack. When  $-20^\circ < \alpha < 95^\circ$ ,  $C_{m\alpha} < 0$ , the starship is longitudinally stable; when  $\alpha = 95^\circ$ ,  $C_{m\alpha} = 0$ , the starship is in neutral static stability, and at this point, the center of gravity and the focus coincide; when  $\alpha > 95^\circ$ ,  $C_{m\alpha} > 0$ , is statically unstable longitudinally. At this time, the longitudinal static stability margin of the starship body needs to be analyzed, which needs to be estimated in combination with the lift derivative  $C_{L\alpha}$  (reflected in the following sections). When  $-20^\circ < \alpha < 10^\circ$  and  $C_{l\beta} > 0$ , the static roll is unstable. When  $\alpha > 10^\circ$  and  $C_{l\beta} < 0$ , static roll is stable. In the measured angle of attack range,  $C_{n\beta} > 0$ , the starship has directional static stability.

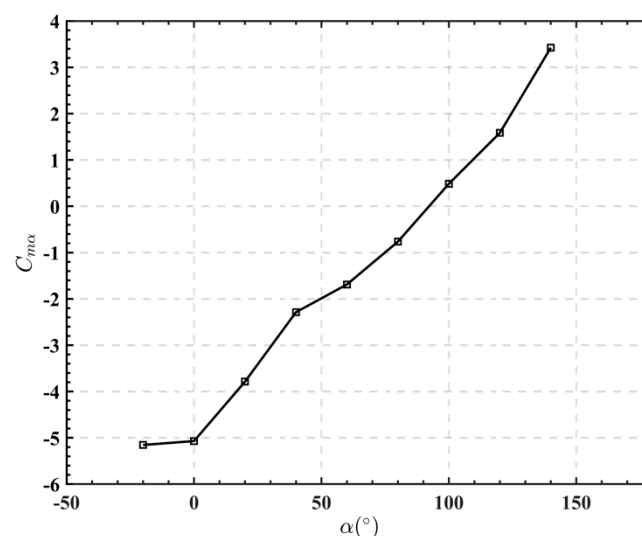


Figure 11. Pitch static stability coefficient.

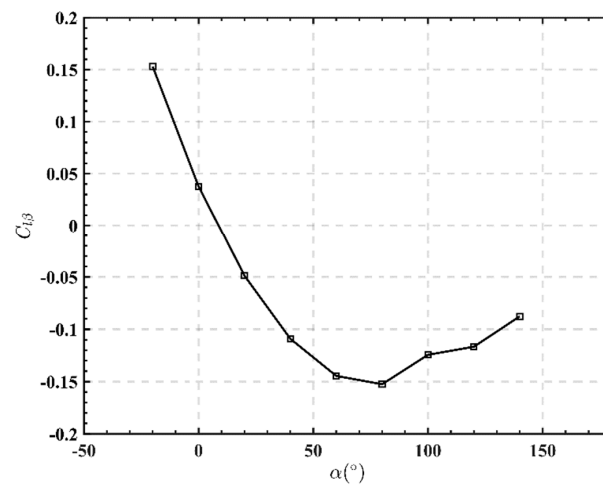


Figure 12. Roll static stability coefficient.

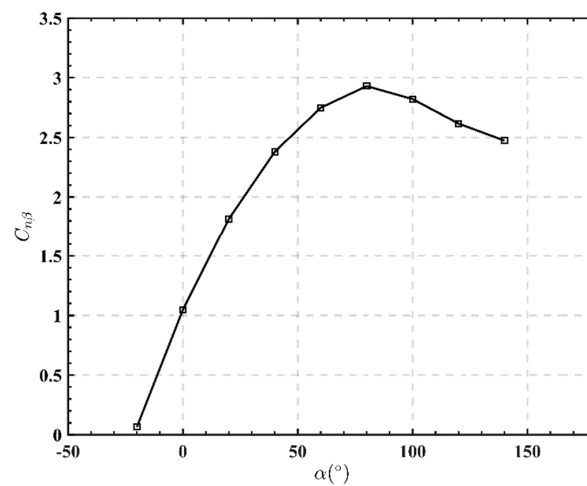


Figure 13. Yaw static stability coefficient.

## 4. Analysis of Dynamic Characteristics

### 4.1. Analysis of Dynamic Derivatives

The dynamic derivative is mainly the variation of the derivative of the dimensionless moment with angle of attack measured at different angles of attack when all rudder surfaces are neutral through the oscillating balance experiment, as shown in Figures 14–16.

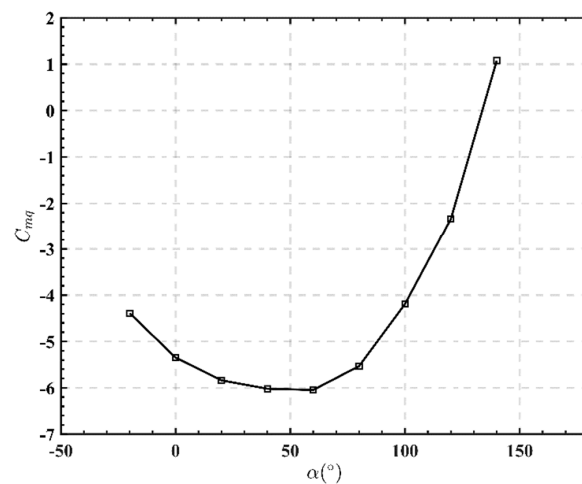


Figure 14. Pitch damping derivative.

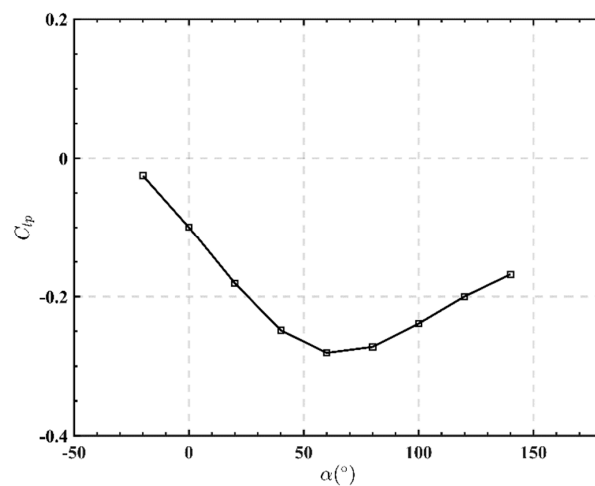


Figure 15. Roll damping derivative.

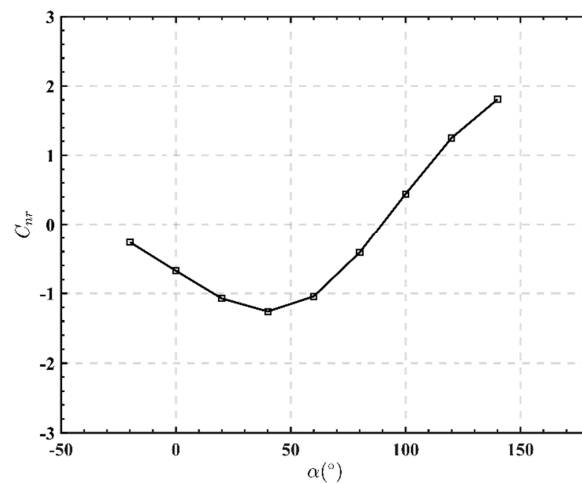


Figure 16. Yaw damping derivative.

It can be seen from the figures that in the range of angle of attack  $-20^{\circ} < \alpha < 90^{\circ}$  in the starship recovery stage, the dynamic derivative conforms to the actual flight characteristics.

- (1) When a starship raises its head and generates a positive pitch angular rate,  $q > 0$ , a starship will also generate a negative pitch moment to prevent it from rotating upwards. Therefore, in Figure 13, within the angle of attack  $-20^{\circ} < \alpha < 135^{\circ}$ , the pitch damping derivatives are all negative, preventing the starship from rotating. When  $\alpha > 135^{\circ}$ , the pitching damping is positive. This is because under a large angle of attack, because the air flow is in chaos, the polarity of the roll moment changes. As a result, during the horizontal descent in the returning stage, the largest angle of attack of the starships is  $90^{\circ}$  according to the analysis of its movement mode and path, so within its range of angle of attack during its movement process, its pitch damping derivative is negative all the time, which conforms to the actual flight characteristics.
- (2) If the starship rolls to the right,  $p > 0$ , the left and right rear wings are asymmetrically deflecting at this time, and a negative roll moment will be generated, which will hinder the roll. Within the whole range of angle of attack, the negative roll moment derivative is exactly caused by the roll angular rate, so the roll damping derivative is consistent with the actual flight characteristics.
- (3) The yaw damping derivative is negative in the range of angle of attack  $-20^{\circ} < \alpha < 90^{\circ}$ , but positive in the range of  $\alpha > 90^{\circ}$ , which promotes the yaw of the starship. Therefore, this phenomenon is easy to cause the risk of excessive yaw in the recovery stage. According to the analysis, the yaw damping derivative conforms to the actual flight

characteristics in the range of a small angle of attack, but in the process of a large angle of attack, it is underdamped.

#### 4.2. Analysis of Manipulativenness Derivative

##### 4.2.1. Pitching Manipulativenness Derivative

When the deflection of elevator-like is positive,  $\delta_e > 0$ , this will destroy the balance of the original star trek. Elevator-like is subject to an upward force, which lies behind the center of gravity, which will produce a negative pitch moment, so regular pitch control derivative angle of attack  $C_{m\delta_e}$  should be negative, and based on analysis, the pitch control derivative shown in Figure 17 is in line with actual flight characteristics.

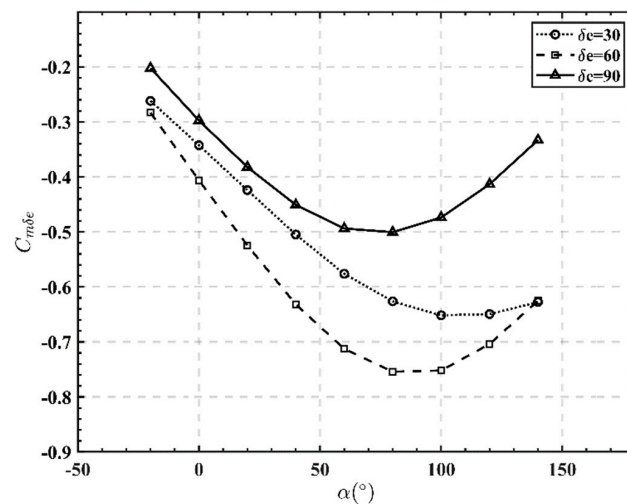


Figure 17. Pitch manipulation derivative.

##### 4.2.2. Rolling Manipulativenness Derivative

It can be seen from Figures 18 and 19 that when the aileron-like wing deflects along the positive direction,  $\delta_a > 0$ , a negative rolling moment is generated, so the rolling control derivative  $C_{l\delta_a}$  is negative. When the rudder-like is deflecting along the positive direction,  $\delta_r > 0$ , a positive side force is generated. Because the rudder-like is located above the axis of the arrow body, a positive rolling moment is generated. Therefore, the cross-control derivative of rudder-like  $C_{l\delta_r}$  is positive, which is consistent with the actual flight situation.

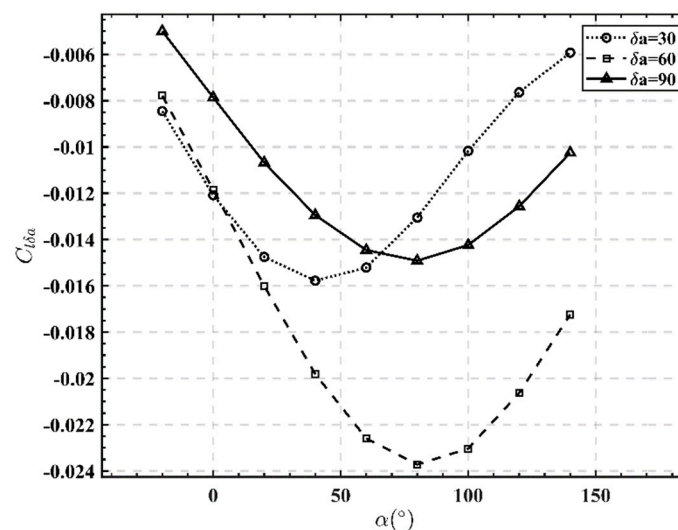


Figure 18. Roll manipulation derivative.

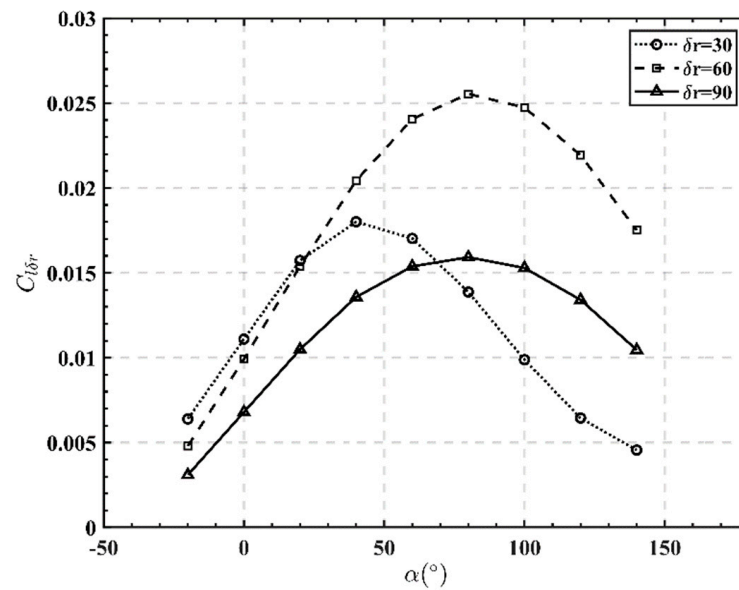


Figure 19. Roll crossover derivative.

#### 4.2.3. Yawing Manipulateness Derivative

It can be seen from Figures 20 and 21 that when the rudder-like is positively deflected,  $\delta_r > 0$ , a positive side force is generated, and then a negative yaw moment is generated, so the yaw control derivative  $C_{n\delta_r}$  is negative. When the aileron is positively deflected, because the starship is facially symmetrical in aerodynamic layout, it will produce the yaw moment by coupling rudder-like and making it deflect. The positive deflection of aileron-like produces negative roll torque, and the resultant force of lift force and gravity makes it sideslip negatively. In order to offset the negative sideslip, rudder-like will produce a positive yaw moment, so the yaw cross-manipulation derivative is  $C_{n\delta_a}$  positive, which is consistent with the actual flight situation.

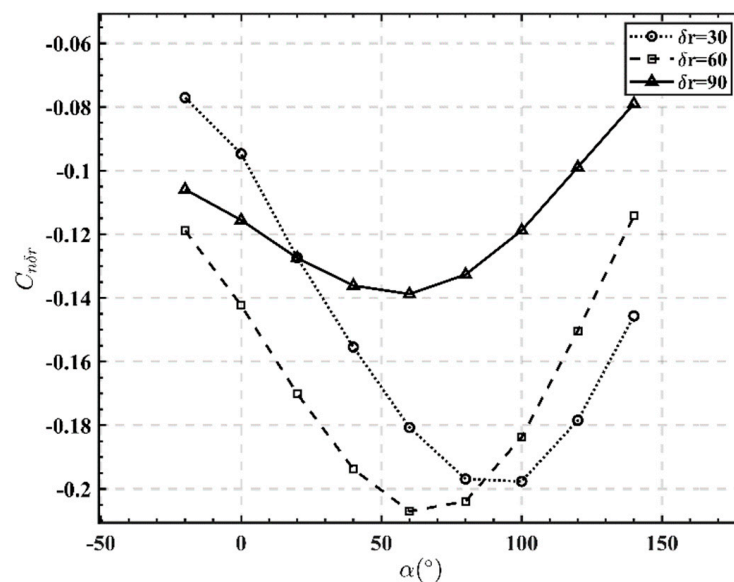


Figure 20. Yaw manipulation derivative.

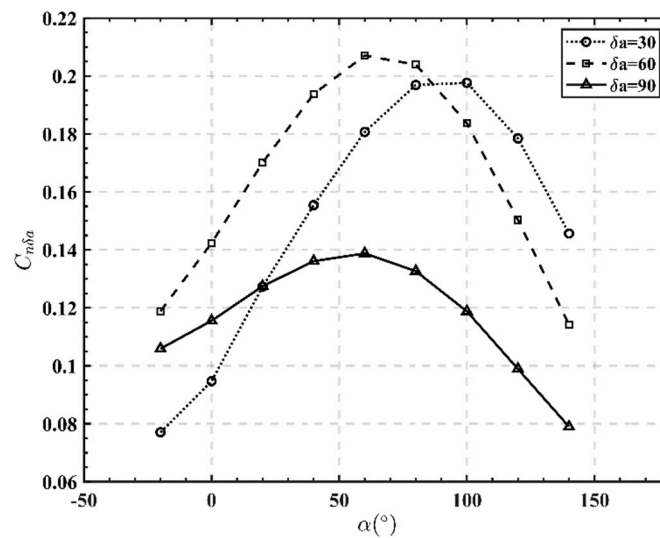


Figure 21. Yaw crossover derivative.

#### 4.3. Analysis of Modal Characteristics and Flight Quality

Similar to the aircraft with the flying wing layout, the starship, with the design of wing-fuselage fusion is a facially symmetrical aircraft from which the vertical tails are canceled, so the dynamic stability analysis method of conventional aircraft is adopted in its dynamic stability analysis [31]. The longitudinal and lateral-directional linearized small disturbance state equations are shown in (1)–(5) and (6), respectively.

$$\dot{x} = Ax + Bu \quad (1)$$

$$x = [\Delta V \quad \Delta \alpha \quad \Delta q \quad \Delta \theta]^T \quad (2)$$

$$u = [\Delta \delta_e \quad \Delta \delta_T]^T \quad (3)$$

$$A = \begin{bmatrix} X_V & X_\alpha + g & 0 & -g \\ -Z_V & -Z_\alpha & 1 & 0 \\ M_V - M_{\dot{\alpha}} Z_V & M_\alpha - M_{\dot{\alpha}} Z_\alpha & M_q - M_{\dot{\alpha}} & 0 \\ 0 & 0 & 1 & 0 \end{bmatrix} \quad (4)$$

$$B = \begin{bmatrix} X_{\delta_e} & X_{\delta_T} \\ -Z_{\delta_e} & -Z_{\delta_T} \\ M_{\delta_e} - M_{\dot{\alpha}} Z_{\delta_e} & M_{\delta_p} - M_{\dot{\alpha}} Z_{\delta_T} \\ 0 & 0 \end{bmatrix} \quad (5)$$

$$\begin{bmatrix} \dot{\beta} \\ \dot{p} \\ \dot{r} \\ \dot{\phi} \end{bmatrix} = \begin{bmatrix} Y_\beta & \alpha_* - Y_p & Y_r - 1 & \frac{g \cos \theta_*}{V_*} \\ L_\beta & L_p & L_r & 0 \\ N_\beta & N_p & N_r & 0 \\ 0 & 1 & \tan \theta_* & 0 \end{bmatrix} \begin{bmatrix} \beta \\ p \\ r \\ \phi \end{bmatrix} + \begin{bmatrix} 0 & L_{\delta_a} \\ L_{\delta_a} & L_{\delta_a} \\ N_{\delta_a} & N_{\delta_r} \\ 0 & 0 \end{bmatrix} \begin{bmatrix} \delta_a \\ \delta_r \end{bmatrix} \quad (6)$$

The definition and expression of each parameter in the formula can be found in the literature [31]. The above equation was used to calculate the characteristic roots of the starship at the trimming angle of attack and compared with the motion characteristic roots of B747 and a flying wing aircraft. Then, the analysis in coordination with the flight quality of GJB-185-86 is shown below.

#### 4.3.1. Longitudinal Analysis

The characteristic equation of the longitudinal overall motion of the starship is calculated by Equations (1)–(5):

$$s^4 + 2.119s^3 + 5.102s^2 + 0.09367s + 5.601e^{-14} = 0 \quad (7)$$

The lateral-directional motion characteristic roots of the starship were obtained as shown in Table 1 and compared with the longitudinal characteristic roots of B747 [26] and a flying wing aircraft [26].

**Table 1.** Longitudinal motion characteristic root comparison.

B747	Flying Aircraft	Starship
$-0.4650 + 1.2456i$	$-1.6$	$-1.05 + 1.99i$
$-0.4650 - 1.2456i$	$0.7$	$-1.05 - 1.99i$
$-0.0097 + 0.0445i$	$-0.01 + 0.12i$	$-5.98 \times 10^{-13}$
$-0.0097 - 0.0445i$	$-0.01 - 0.12i$	$-0.0185$

It can be seen from Table 1 that the characteristic roots are all located in the negative half-plane, indicating that the longitudinal motion is stable. In addition, the characteristic roots are composed of a pair of conjugate complex roots and two negative real roots. It is easy to find that the long-period mode degenerates into the negative real roots of the third mode, which is between the long and short periods. When the starship is in longitudinal motion, due to the shaking fuel, the center of gravity moves backward, and static stability is decreased, which makes the pitching moment and frequency increase, the damping ratio increase, the imaginary part of the long-period mode slowly change into zero, and the characteristic roots of long-period mode degenerate into two different negative real roots. The starship is overdamped, and the motion response is exponentially and monotonously convergent, indicating that the longitudinal motion is stable.

There is also a method [33] to estimate the characteristic roots of long-period mode according to the balance state quantity without considering the influence of compressibility and the change of thrust velocity. In engineering, there is little error between the result of this method and that of the fourth-order equation. The formula is shown as follows:

$$\begin{cases} \omega_{n,p} = \sqrt{2} \frac{g}{u_0} \\ \zeta_p = \frac{1}{\sqrt{2}(C_L/C_D)} \\ \lambda_p = -\zeta_p \omega_{n,p} \pm i \omega_{n,p} \sqrt{1 - \zeta_p^2} \end{cases} \quad (8)$$

After substituting the balance state quantity, the long-period modal characteristic roots  $-0.06 \pm 0.24475i$  are obtained as Table 2 and the standard characteristics are listed as Table 3.

From the above analysis, it can be seen that the third mode of the starship converges exponentially, the short period mode meets the requirement of level 1 flight quality, and the estimated long-period modes before modal degradation also meet the requirement of flight quality of level 1.

**Table 2.** Modal characteristics of longitudinal course motion.

Mode	$T_{1/2}/s$	$T/s$	$N_{1/2}/\text{Circle}$	$\zeta$	$\omega_n$
Third mode	37.46	—	0	1	0.0185
Short mode	0.66	3.157	0.209	0.4667	2.25
Estimation long-period	11.55	25.671	0.4499	0.2381	0.252

**Table 3.** GJB-185-86 longitudinal modal characteristic standard.

Mode	Level of Flight Quality	Type of Aircraft	Maximum of $\zeta$	Minimum of $\zeta$
Short mode	1	C	1.30	0.35
	2		2.00	0.25
	3		—	0.15
Long mode	1	C	$\zeta > 0.04$	
	2		$\zeta > 0$	
	3		$T_2 > 55s$	

4.3.2. Lateral-Directional Analysis

Through calculation of Equation (6), the characteristic equation of the starship’s lateral-directional overall motion is:

$$s^4 - 0.00956s^3 - 0.04901s^2 + 0.02285s + 0.0001024 = 0 \tag{9}$$

The characteristic roots of lateral-directional motion of the starship are shown in Table 4 and are compared with those of B747 [27] and a flying wing aircraft [27].

**Table 4.** Lateral heading motion characteristic root comparison.

B747	Flying Aircraft	Starship
-0.1507 + 0.9431i	0.025 + 0.35i	0.175 + 0.195i
-0.1507-0.9431i	0.025-0.35i	0.175-0.195i
-0.3725	-2.0000	-0.336
0.0058	0.0006	-0.00444

It can be seen from the table that the starship and the flying wing aircraft have no vertical tails, so their  $C_{n\beta}$ , which plays a role in the recovery of Dutch rolling motion, is small, and it is the same thing with  $C_{nr}$  and  $C_{s\beta}$ , which play a role in damping. Moreover, because the  $C_{l\beta}$  is also small,  $C_{l\beta}$  will be too large, so the directional damping is further reduced, resulting in the instability of the Dutch roll mode. Because the starship’s spiral mode, lying in the left of the imaginary axis is close to its imaginary axis, and its roll mode is also located at the left of the imaginary axis, it could be approximately assumed that its roll and spiral modes are stable.

According to the comparison between Tables 5 and 6, the rolling mode of the starship meets level 2 flight quality, and the spiral mode meets level 1 flight quality. A pair of conjugate complex roots corresponding to the Dutch roll mode is in the right plane and in an unstable state. Considering the aerodynamic derivative affecting the Dutch roll mode in the above analysis,  $C_{n\beta}$ ,  $C_{nr}$ ,  $C_{s\beta}$ ,  $C_{n\delta_r}$ , and  $C_{l\delta_r}$  should be added to improve the Dutch roll mode, but it should be considered that the impact of  $C_{l\beta}$  on the Dutch rolling is relatively small, and the ratio relationship of  $C_{l\beta}$  and  $C_{n\beta}$  should be considered when improving its value to avoid affecting the stability of the spiral mode.

**Table 5.** Modal characteristics of lateral course motion.

Parameters	Rolling Time Constant $T_R/s$	Spiral Amplitude Doubling Time $T_2/s$	Natural Frequency of Dutch Roll $\omega_d$	Damping Ratio of Dutch Roll $\zeta_d$	$\omega_d \cdot \zeta_d$
Value	2.98	225	0.669	0.261	0.175

**Table 6.** GJB-185-86 lateral modal characteristic standard.

Parameters	Standards of Flight Quality	Type of Flight Stage	Type of Aircraft	Maximum of $T_R/s$	Minimum of $T_2/s$	Minimum of $\omega_d$	Minimum of $\zeta_d$	Minimum of $\omega_d \cdot \zeta_d$
Value	I	C	II	1.4	20	0.4	0.08	0.15
	II			3.0	12	0.4	0.02	0.05
	III			10	4	0.4	0.02	—

#### 4.4. Characteristics Analysis of the Ratio between Roll and Swing

In the literature [34], the ratio between roll and swing  $|\phi/\beta|_d$  is used to represent the proportion of rolling motion and yaw motion in the Dutch roll mode, and a large ratio between roll and swing means that the proportion of rolling motion in the Dutch roll mode is large. A small ratio between roll and swing indicates that the yaw motion accounts for a large proportion of the Dutch roll mode.

$|\phi/\beta|_d$  is the amplitude of the eigenvector ratio of roll angle and sideslip angle that corresponds to the eigenvalue of Dutch roll, and the approximate expression is shown as follows:

$$\left| \frac{\phi}{\beta} \right| \cong \left| \frac{L'_\beta}{\omega_d} \right| \frac{1}{\sqrt{1 + L'_p{}^2/\omega_d^2}} \quad (10)$$

For the flight state of high angle of attack,  $\omega_d^2 \approx N'_\beta \cos \alpha - L'_\beta \sin \alpha$ , the approximate expression is transformed into:

$$\left| \frac{\phi}{\beta} \right| \cong \left| \frac{L'_\beta}{N'_\beta \cos \alpha - L'_\beta \sin \alpha} \right| \frac{1}{\sqrt{1 + L'_p{}^2/(N'_\beta \cos \alpha - L'_\beta \sin \alpha)}} \quad (11)$$

where  $L'_\beta$  is the dominant torque of sideslip angle on the body axis roll,  $N'_\beta$  is the dominant number of yaw moment of body axis caused by the sideslip angle, and  $L'_p$  is the dominant torque of the roll angle rate on the body axis.

During the glide stage at a high angle of attack,  $L'_\beta/N'_\beta$  is smaller, and  $L'_p$  is large and has a smaller ratio between roll and swing. Shown in Figure 22 is the roll and swing ratio of each state quantity calculated according to the linear model with small disturbance at a high angle of attack, and it is about 0.0001 under a large angle of attack. Under a small roll and swing ratio, the Dutch roll mode of the starship is mainly reflected by yaw motion.

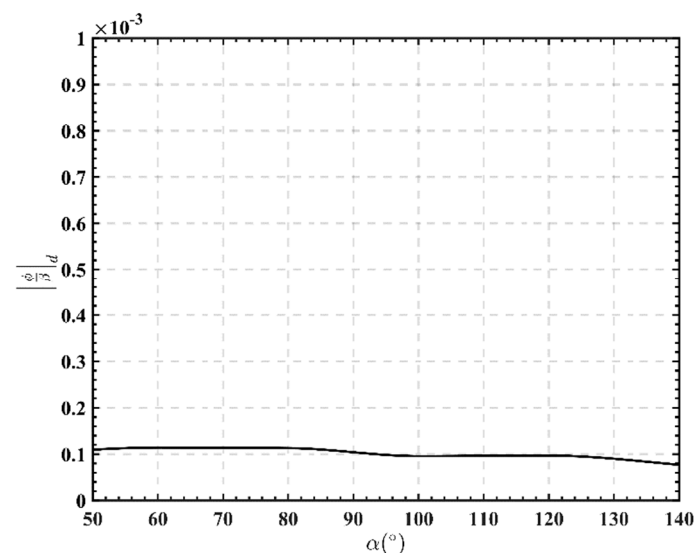


Figure 22. Roll–Sideslip ratio.

## 5. Analysis Based on the Principle of Criteria

### 5.1. Criteria of the Margin of Longitudinal Static Stability

Since the layout of starships is similar to that of flying wing aircraft and winged missiles, the longitudinal static stability margin of a traditional aircraft can be used to judge whether it is longitudinally stable or not. Its formula is defined as follows:

$$K_\alpha = -\frac{\partial C_m}{\partial C_L} = -\frac{C_{m\alpha}}{C_{L\alpha}} = x_F - x_G \quad (12)$$

where  $C_m$  and  $C_{m\alpha}$  are the pitching moment coefficient and the pitching static stability derivative, respectively;  $C_L$  and  $C_{L\alpha}$  are the lift coefficient and the lift derivative, respectively;  $x_F$  and  $x_G$  are the dimensionless focus position and the center of gravity position, respectively.

That  $K_\alpha$  is positive ( $K_\alpha > 0$ ) indicates that the focus is behind the center of gravity, which is statically stable in longitudinal direction; conversely,  $K_\alpha < 0$  indicates that the focus is in front of the center of gravity, which is statically unstable in longitudinal direction. Figure 23 shows that  $K_\alpha$  is positive all the time when  $-20^\circ < \alpha < 92^\circ$ , and it is negative when  $\alpha > 92^\circ$ , turning statically unstable. In actual flight, because the body of the arrow is elastic and with the consumption and shaking of the fuel [32], with the increase in the angle of attack, in the condition of a small angle of attack, the center of gravity shifts back and forth, and the static stability margin coefficient of the center of gravity also fluctuates, which is shown as follows. At a high angle of attack, the center of gravity moves backward, and the starship changes from statically stable in the longitudinal direction to statically unstable. However, at a high angle of attack, the static instability coefficient is small and meets the requirements of controllability [18]. Therefore, the longitudinal stability augmentation control law and controller should be designed, and the constraint range should be given to assist the longitudinal stability augmentation of the starship when it moves at a high angle of attack.

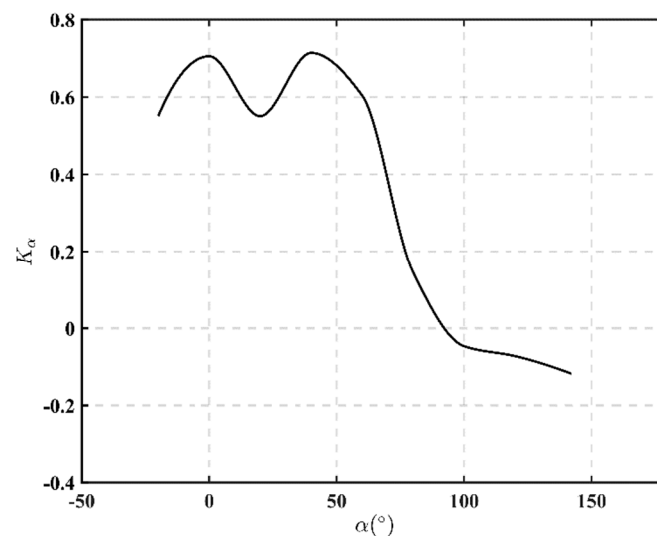


Figure 23. Longitudinal static stability margin.

### 5.2. Criteria of Comprehensive Analysis of Lateral Direction

This criterion can effectively evaluate the lateral-directional deviation and motion characteristics of a starship by the comprehensive analysis of dynamic directional stability criterion  $C_{n\beta dyn}$  and lateral steering deviation stability criterion  $LCDP$ . Figure 24 shows the graph of analysis results of dynamic deviation and lateral control stability criteria.

$$C_{n\beta dyn} = C_{n\beta} \cos \alpha - \frac{I_z}{I_x} C_{l\beta} \sin \alpha \quad (13)$$

where  $C_{n\beta dyn}$  is the dynamic direction stability deviation parameter;  $I_x$ ,  $I_z$  are, respectively, the inertial moment along the x-axis and the inertial moment along the z-axis.  $C_{n\beta dyn} > 0$  indicates that the aircraft has dynamic directional stability; otherwise, it does not.

$$LCDP = C_{n\beta} - C_{l\beta} \frac{C_{n\delta a}}{C_{l\delta a}} \quad (14)$$

where  $LCDP$  is the lateral manipulation deviation parameter.  $LCDP > 0$  indicates that there is no deviation in lateral-directional control; on the contrary, it means that there is deviation in lateral-directional control.

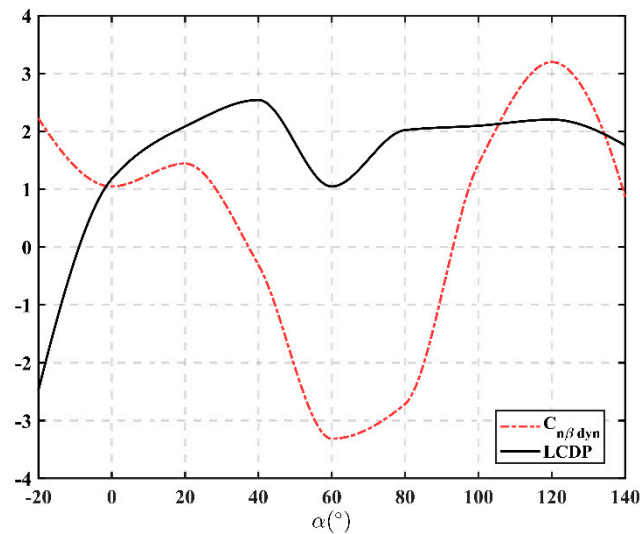


**Figure 24.** Comprehensive analysis of dynamic deviation and lateral control stability criteria.

As can be seen from the figures, when the angle of attack is at  $-20^\circ < \alpha < -10^\circ$ ,  $C_{n\beta dyn} > 0$ ,  $LCDP < 0$ , because the absolute value of the deviation parameter of dynamic yaw stability is larger than that of the lateral control deviation parameter, sideslip can also be eliminated by rolling motion of aileron-like without deviation. When the angle of attack is  $-10^\circ < \alpha < 38^\circ$  and  $\alpha > 93^\circ$ ,  $C_{n\beta dyn} > 0$  and  $LCDP > 0$ , if sideslip occurs due to external interference at this time, the starship is stable laterally and the reverse pressure bar can also eliminate sideslip, so there will not be sideslip deviation phenomenon to endanger the starship. When  $38^\circ < \alpha < 93^\circ$ ,  $C_{n\beta dyn} < 0$ , and  $LCDP > 0$ , there will be the phenomenon of control backlash. However, in the range of  $38^\circ < \alpha < 45^\circ$  and  $88^\circ < \alpha < 93^\circ$ , because the absolute value of the lateral control deviation parameter is larger than that of the deviation parameter of dynamic yaw stability, yaw coupling brought by the rolling maneuver of aileron-like roll can also eliminate sideslip. When  $45^\circ < \alpha < 88^\circ$ , the absolute value of the deviation parameter of dynamic yaw stability is larger than that of the lateral control deviation parameter, or there is little difference between them. If sideslip occurs at this time, sideslip cannot be quickly eliminated; if the operation stick is reversed, there will be an anticontrol phenomenon.

### 5.3. Analysis Criteria of Coordinated Control Deviation of Rudder-like and Aileron-like

In the  $LCDP$  criterion, only the operation of aileron-like is considered, and the rudder-like is in neutral state, while in the actual flight condition, aileron-like and rudder-like are in coordination to realize horizontal directional movement. As a result, the parameters quantity of rudder-like control are also introduced into the analysis of control deviation, forming a new deviation analysis criterion of coordinated control of rudder-like and aileron-like, which is shown as follows:

$$LCDP_{ARI} = C_{n\beta} - C_{l\beta} \frac{C_{n\delta_a} + kC_{n\delta_r}}{C_{l\delta_a} + kC_{l\delta_r}} \quad (15)$$

$$k = \frac{\delta_r}{\delta_a} \quad (16)$$

where  $LCDP_{ARI}$  is the coordinated control deviation parameter of aileron-like and rudder-like. Similar to the lateral steering deviation stability criterion, when  $LCDP_{ARI} > 0$ , the

rudder-like and aileron-like coordinated control is stable in operation; otherwise, it is not stable.

According to Figure 25, when the value of  $k$  is larger, the range of angle of attack with the coordinated control deviation parameter, which is more than zero increases, indicating that the stability of rudder-like and aileron-like coordinated control is much better than that of rudder-like or aileron-like control alone. When  $k = 1/3$ , within the angle of attack range of  $-20^\circ < \alpha < 0^\circ$  and  $25^\circ < \alpha < 55^\circ$ , the coordinated control deviation parameter is negative, while in the angle of attack range of  $0^\circ < \alpha < 25^\circ$  and  $\alpha > 55^\circ$ , the coordinated control deviation parameter is positive. When  $k = 0.5$ , the coordinated control deviation parameter is negative within the angle of attack range of  $-20^\circ < \alpha < -5^\circ$  and  $32^\circ < \alpha < 50^\circ$ , while the coordinated control deviation parameter is positive within the range of  $-5^\circ < \alpha < 32^\circ$  and  $\alpha > 50^\circ$ . When  $k = 2/3$ , the coordinated control deviation parameter is negative within the range of  $-20^\circ < \alpha < -15^\circ$ , and the parameter is positive within the range of  $\alpha > -15^\circ$ . When  $k = 1$ , the deviation parameters of coordinated control are all positive in all angle of attack ranges, indicating that when the deflection angles of rudder-like and aileron-like are the same, the best control effect of coordinated operation is achieved.

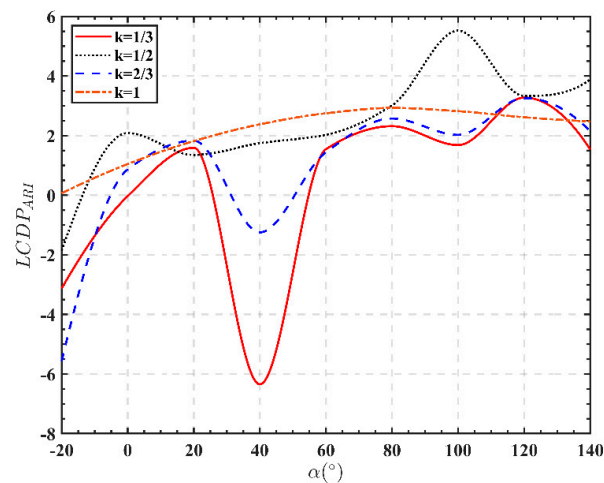


**Figure 25.** Evolution of parameters  $LCDP_{ARI}$  versus angle of attack (AoA) when  $k$  takes different positive values.

As can be seen from Figure 26, when different negative values of  $k$  are taken, the deviation parameters change little, and the effect is of little difference to that of the  $LCDP$  criterion. Therefore, when different negative values of  $k$  are taken, the rudder-like cannot compensate the aileron-like.

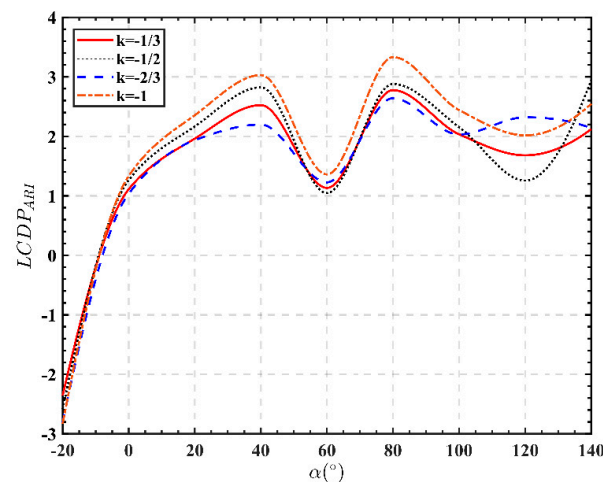


**Figure 26.** Evolution of parameters  $LCDP_{ARI}$  versus AoA when  $k$  takes different positive values.

#### 5.4. Weissman Graph Criteria

According to reusable carriers Weissman criterion that is introduced in the literature [35,36], the distribution of typical lateral-directional aerodynamic characteristics state points of the coordinated control of rudder-like and aileron-like of the starship in horizontal slip returning on the Weissman graph was analyzed. What is shown in Figure 27a is the Weissman diagram after the boundary was updated in 1980, and Figure 27b is the distribution diagram of the lateral-directional aerodynamic characteristics points on Weissman.

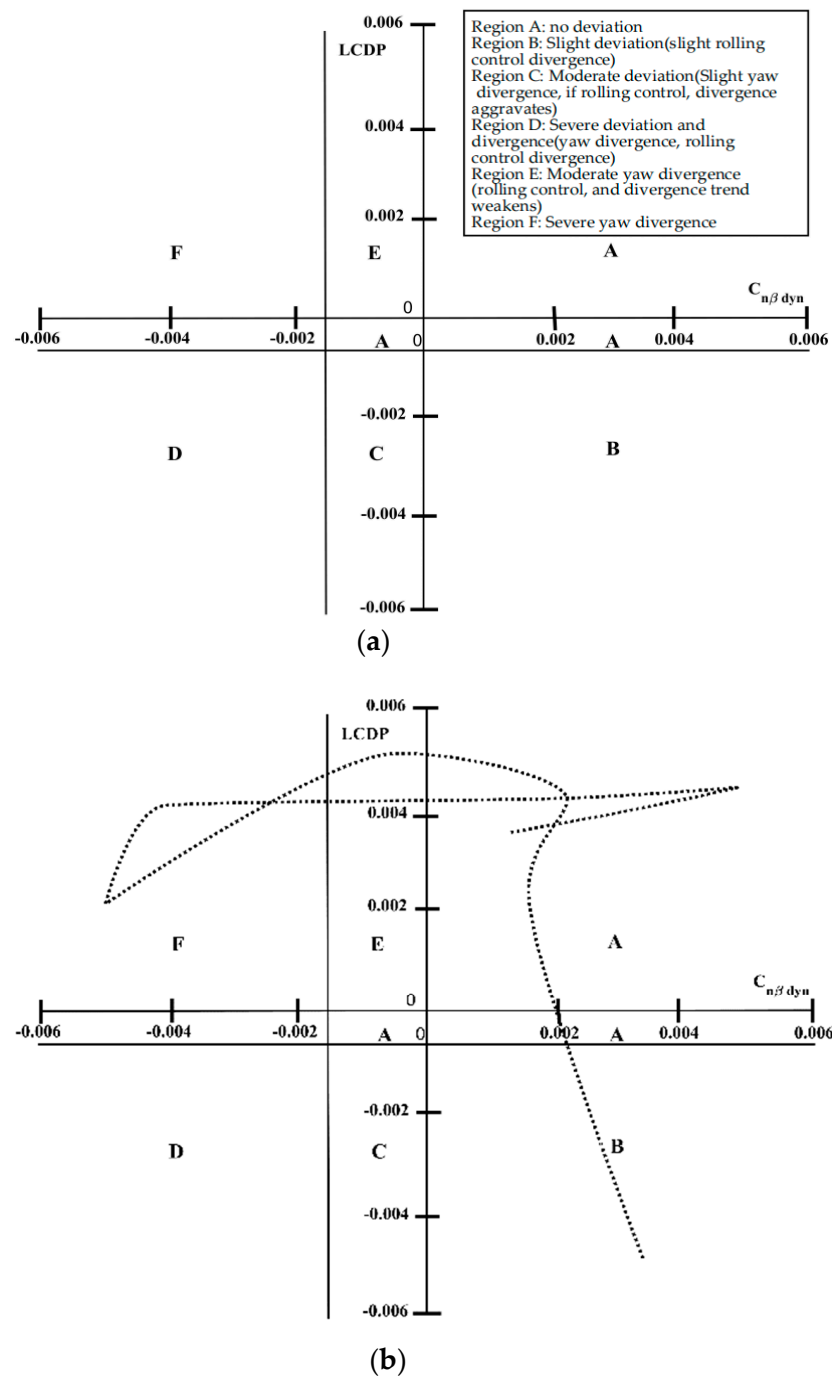


**Figure 27.** Weissman. (a) The Weissman diagram with updated boundary. (b) the distribution diagram of the lateral-directional aerodynamic characteristics points on Weissman.

In the figures, Region A is the no-deviation zone, Region B is a slight-deviation zone, Region C is a moderate-deviation zone, Region D is a heavy-deviation zone, Region E

is a moderate -yaw -divergence zone (roll control is carried out, and divergence trend is weakened), and Region F is the strong -yaw -divergence zone.

Figure 27b shows that most states of starship lie in Area A, without lateral-directional deviation, and a portion of the state points falls in Area F, because during the returning stage with a large angle of attack, horizontal directional movement may be unstable, so the directional stabilization augmentation controller should be designed to move Area F overall to the right to Area E or the controllable part of Area A. There are only a few cases of slight yaw or divergence of rolling in the figure, and the divergence can be weakened by mutual compensation control.

## 6. Simulation Results of Nonlinear Open Loop

### 6.1. Longitudinal Simulation Results

Now the accuracy of the above analysis results has been verified by the time response simulation of the starship scaling model under  $V = 60 \text{ m/s}$ ,  $H = 3000 \text{ m}$ . A unit step response is given to the rudder-like when the starship is in the trimming state. The response curves of angle of attack, pitch rate, and pitch angle over time are shown in Figures 28–30.

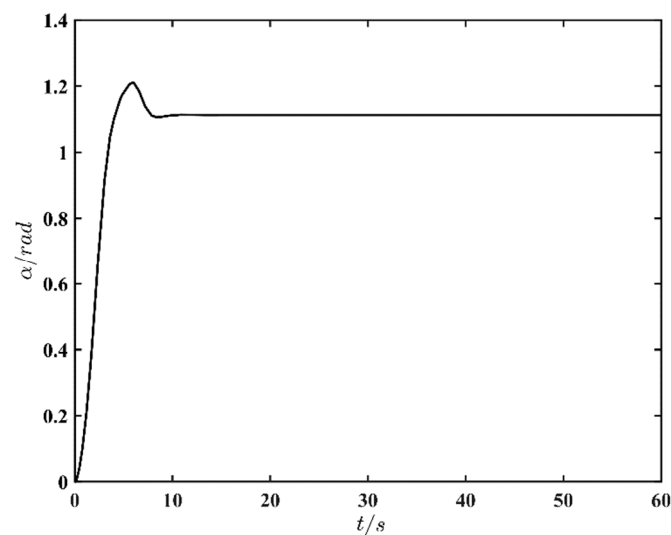


Figure 28. Angle of attack response over time.

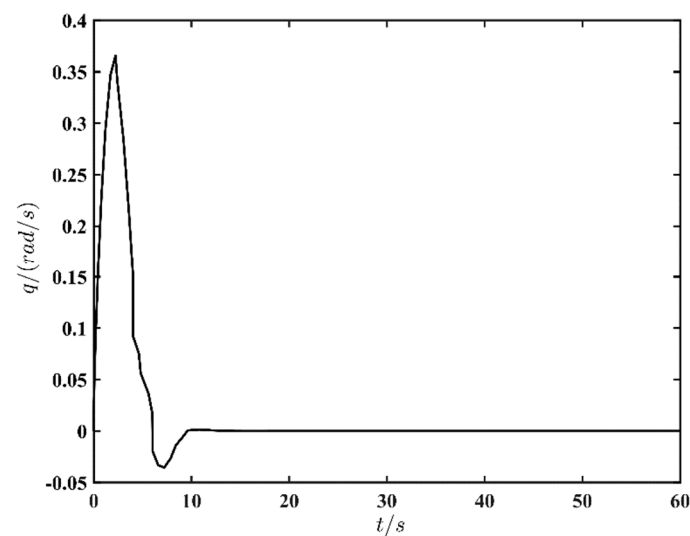


Figure 29. Pitch rate response over time.

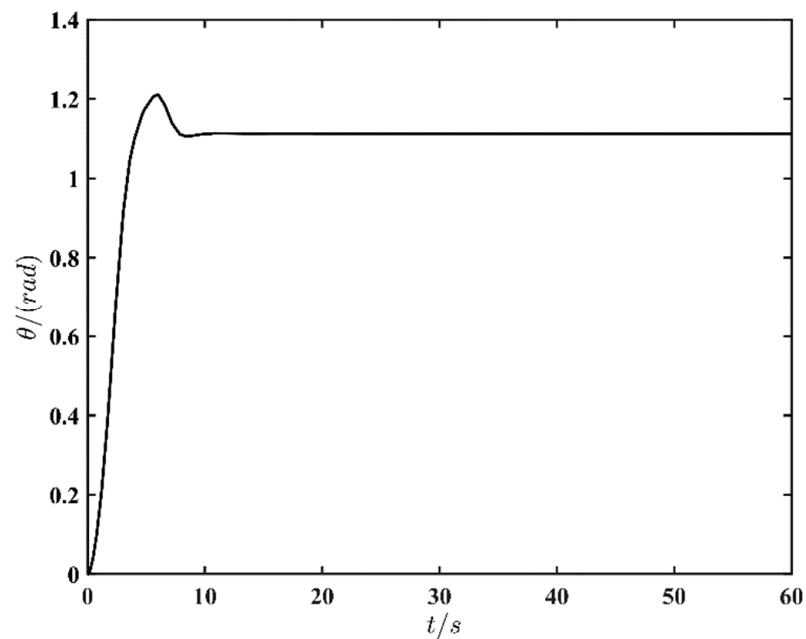


Figure 30. Pitch angle response with time.

It can be seen from the figures that short period characteristics of the starship are obvious during the unit step deflection of elevator-like, whose reflection on the angle of attack and pitch angular rate is that the starship could turn to the stable state quickly. At the same time, from the response curve of the pitch angle over time, the pitch angle also quickly returned to a stable state without accompanying oscillation, indicating that the long period degenerated into the third mode, which is an exponentially monotonous and convergent motion. Therefore, in the perspective of simulation results, it is consistent with the above analysis of control stability characteristics, and it verifies the accuracy of the above analysis.

## 6.2. Lateral-Directional Simulation Results

Now a unit step response is given to the aileron-like under  $V = 60 \text{ m/s}$ ,  $H = 3000 \text{ m}$ ,  $\beta = 0$ , and the original  $p = q = r = 0$  is ensured. The response curves along time of sideslip angle, roll angle, roll angular rate, and yaw angle are shown as follows.

Figures 31–34 show that after a step response is given to aileron-like, because the roll mode belongs to level 2 flying quality, this makes it slow for the roll angle to recover to the stable state. According to Figures 31 and 32, when the aileron-like steps, it takes the rolling angle 30 s to recover to a stable state. Because the lateral force caused by aileron-like deflection is small, coupling yaw motions are also small, and the yaw angle returns faster to the stable state than the roll angle. The starship is short of vertical tails, so its  $C_{n\beta}$ , which plays a role in the recovery of Dutch rolling motion, is small. Moreover, the  $C_{l\beta}$  is also small, which leads the directional damping further reduced, resulting in the instability of the Dutch roll mode. Because the starship's spiral mode is close to its imaginary axis, and its roll mode is also located at the left of the imaginary axis, it could be approximately assumed that its roll and spiral modes are stable. Therefore, the half-life of the roll response is about 0.3 s.

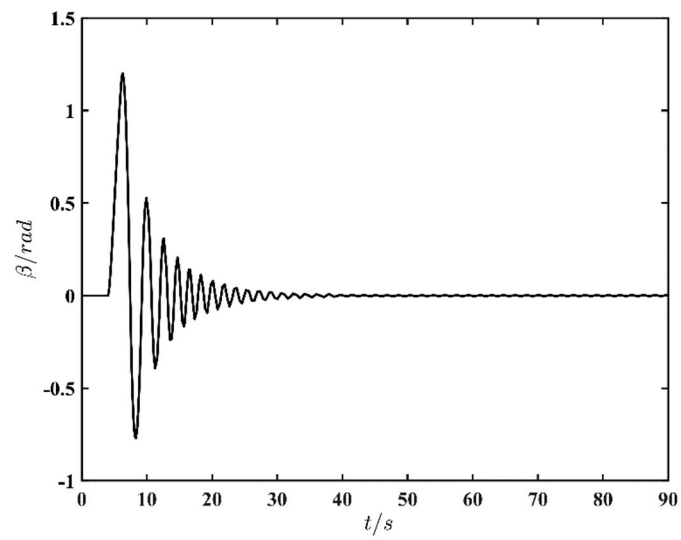


Figure 31. Sideslip angle response over time.

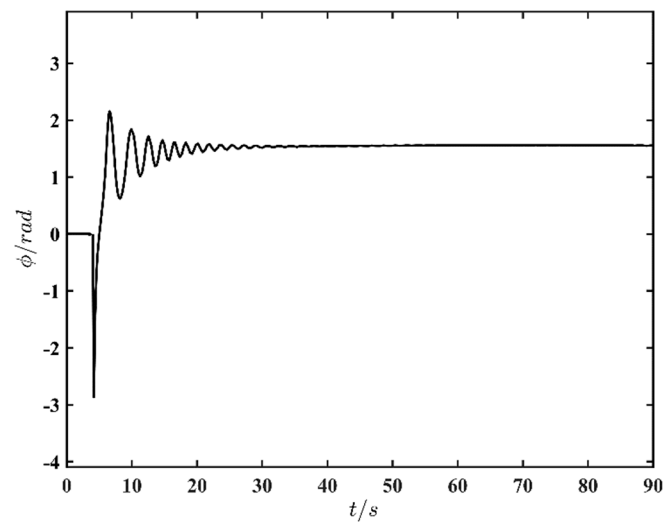


Figure 32. Roll angle response over time.

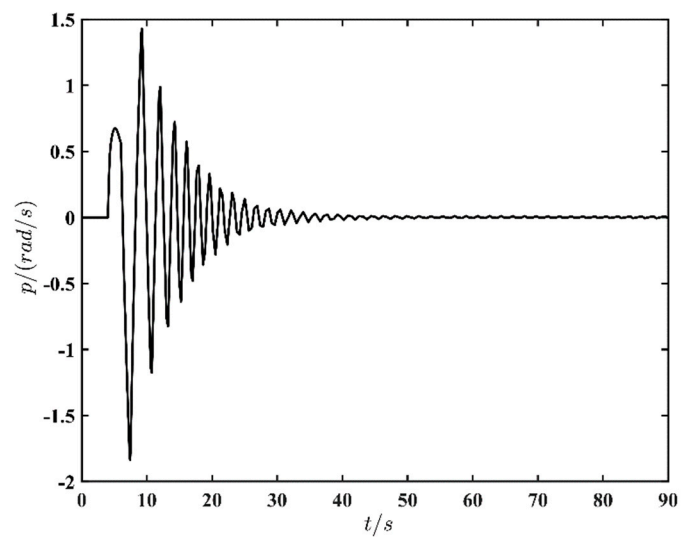
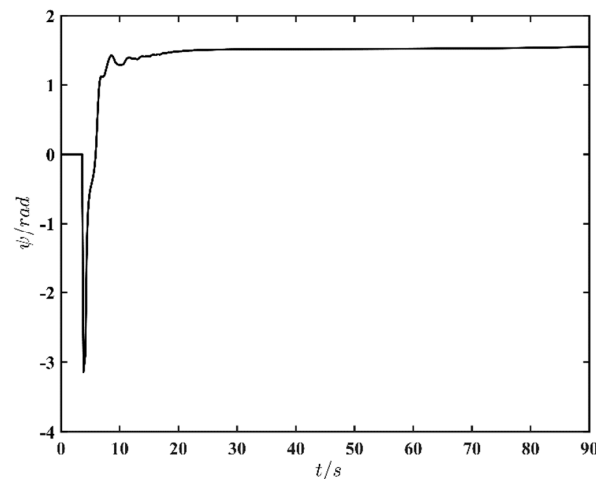


Figure 33. Roll rate response over time.



**Figure 34.** Yaw angle response with time.

Meanwhile, it can be seen from the analysis in the last section that the dynamic instability of the yaw motion of the starship is divergent, and by controlling the aileron, the sideslip could be eliminated, and the divergence trend could be weakened. As can be seen from Figures 30 and 33, the simulation results are consistent with the analysis mentioned in the last section.

Now a unit step response is given to the rudder-like under  $V = 60$  m/s,  $H = 3000$  m,  $\beta = 0$ , and at the same time,  $p = q = r = 0$ , the response curves of sideslip angle, yaw angle, roll angle, and yaw angle rate along the time are shown below.

According to the analysis in the previous section, sideslip can be eliminated by the combined control of aileron-like and rudder-like, so the sideslip angle in Figure 34 can recover to a stable state. However, when the rudder-like steps, the lateral-directional motion wholly diverges, which is caused by the instability of the Dutch roll mode of the starship itself. From the analysis of the roll and swing ratio characteristics in the last segment, it can be seen that the yaw motion accounts for a large proportion of the Dutch roll, so when the rudder-like steps, the yaw motion diverges. Meanwhile, according to the Weissman criterion, some of the state points of the starship fall in the strong yaw divergence zone during lateral-directional motions. It can be concluded that when the rudder-like steps, the simulation results are also consistent with the characteristics analysis. And the response curves, namely, sideslip angle, yaw, roll angle, yaw rate, versus time are showed as Figures 35–38 below.

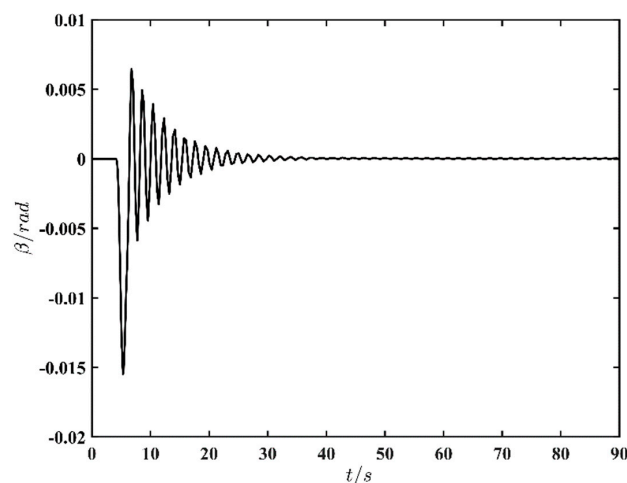


**Figure 35.** Sideslip angle response over time.

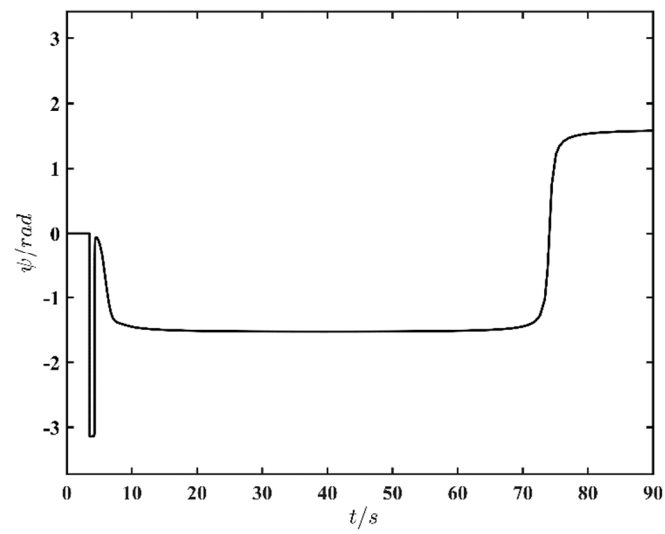


Figure 36. Yaw angle response with time.

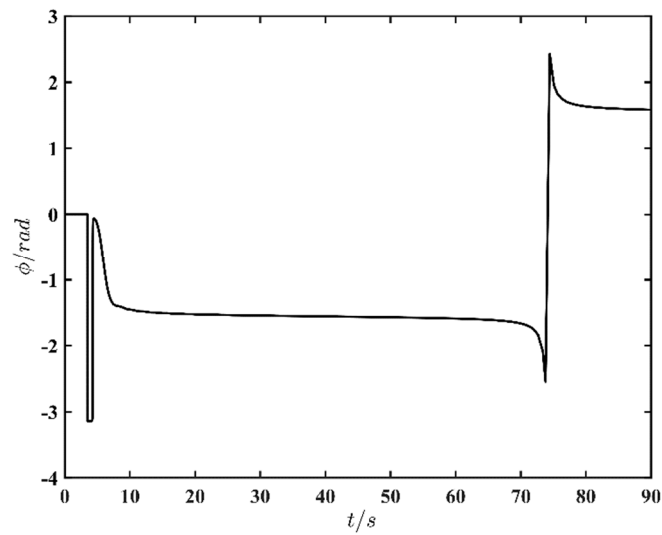


Figure 37. Roll angle response over time.

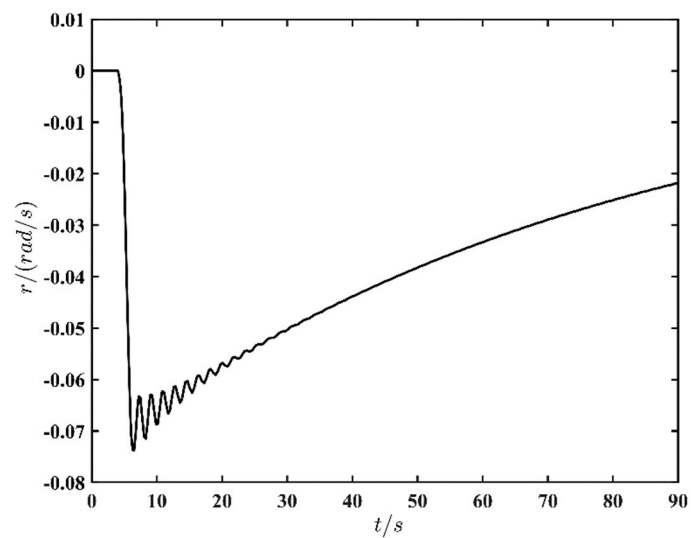


Figure 38. Yaw rate response over time.

As can be seen from the lateral-directional simulation results, the characteristics of the lateral-directional motions are consistent with the lateral-directional characteristics analysis in the previous section.

## 7. Conclusions

After the aerodynamic characteristics analysis, modal analysis, and deviation criterion analysis of the starship, the following conclusions are drawn:

The starship is longitudinally stable when  $-20^\circ < \alpha < 92^\circ$ , and becomes longitudinally statically unstable when  $\alpha > 92^\circ$ , at which time the center of gravity moves to the focus. It does not have rolling static stability when  $-20^\circ < \alpha < 10^\circ$ . When  $\alpha > 10^\circ$ , it has rolling static stability; The starship is always yaw statically stable within the range of angle of attack.

Both long and short longitudinal period mode of the starship meet the level 1 flight quality, and the motion response of the third mode after degradation is exponentially monotonous convergent. The lateral-directional roll mode meets level 2 flight quality, and the spiral mode meets level 1 flight quality. A pair of conjugate complex roots corresponding to the Dutch roll mode is in the right plane, which is in an unstable state. The Dutch roll mode is mainly reflected in yaw motion, which is divergent.

Through the comprehensive analysis of dynamic deviation and lateral control stability criteria, it can be seen that when  $45^\circ < \alpha < 88^\circ$ , if sideslip occurs, the anticontrol phenomenon is easy to occur, thus the design of directional control systems deserves attention.

The effect of combined control of rudder-like and aileron-like is better than that of single control of either rudder-like or aileron-like, and the best control effect is achieved when the compensation gain of rudder-like to aileron-like is 1. When the compensation gain is negative, the rudder-like cannot compensate the aileron-like.

The simulation result of open-loop ontology shows that when a unit step response is given to elevator-like and rudder-like and aileron-like, after the elevator-like and aileron-like step, the starship ontology can recover to a stable state, but after the rudder-like step, the lateral-directional motion of the whole starship diverges, which indicates that the direction of the starship ontology is unstable, and a directional stability augmentation controller is necessary to be designed.

**Author Contributions:** Methodology, Z.L.; formal analysis, C.Y. and M.D.; data curation, C.Z.; writing—original draft preparation, Z.W.; writing—review and editing, Z.G. All authors have read and agreed to the published version of the manuscript.

**Funding:** This research received no external funding.

**Institutional Review Board Statement:** Not applicable.

**Informed Consent Statement:** Not applicable.

**Data Availability Statement:** Not applicable.

**Conflicts of Interest:** The authors declare no conflict of interest.

## Abbreviations

RLV	Reusable Launch Vehicle
CFD	Computational Fluid Dynamics
LCDP	Lateral Control Departure Parameter
AoA	Angle of Attack

## References

1. Britt, R.T.; Arthurs, T.D.; Jacobson, S.B. Aeroservoelastic analysis of the B-2 bomber. *J. Aircr.* **2000**, *37*, 745–752. [[CrossRef](#)]
2. Jacobson, S.; Britt, R.; Freim, D.; Kelly, P. Residual pitch oscillation (rpo) flight test and analysis on the b-2 bomber. *Ices J. Mar. Sci.* **2003**, *67*, 1260–1271.
3. Su, W.; Gao, Z.; Xia, L. Multiobjective optimization design of aerodynamic configuration constrained by stealth performance. *Acta Aerodyn. Sin.* **2006**, *24*, 137–140.

4. Johnson, J.; Colbo, H. Space Shuttle main engine progress through the first flight. In Proceedings of the 17th Joint Propulsion Conference, Colorado Springs, CO, USA, 27–29 July 1981.
5. Klotz, I. SpaceX Aims for Starship Crew Flights By 2023. *Aerosp. Dly. Def. Rep.* **2020**, 272, 3.
6. SpaceX Starship SN8 Takes Flight, 2020. Available online: <https://www.spacex.com/updates/starship-sn8-takes-flight/index.html> (accessed on 10 June 2022).
7. SpaceX. Starship SN9 High-Altitude Flight Test, 2021. Available online: <https://www.spacex.com/updates/starship-sn9-flight-test/index.html> (accessed on 10 June 2022).
8. SpaceX. Starship SN10 High-Altitude Flight Test, 2021. Available online: <https://www.spacex.com/updates/starship-sn10-flight-test/index.html> (accessed on 10 June 2022).
9. SpaceX. Starship SN11 High-Altitude Flight Test, 2021. Available online: <https://www.spacex.com/updates/starship-sn11-flight-test/index.html> (accessed on 10 June 2022).
10. SpaceX. StarShip SN15, 2021. Available online: <https://www.spacex.com/updates/starship-sn15-flight-test/index.html> (accessed on 10 June 2022).
11. Klotz, I. Starship Hop on Hold Pending Demo-2. *Aerosp. Dly. Def. Rep.* **2020**, 272, 2.
12. Norris, G. SpaceX Plans Pacific Splashdown for First Starship Orbital Test. *Aerosp. Dly. Def. Rep.* **2021**, 276, 6.
13. Goman, M.G.; Khramtsovsky, A.V.; Kolesnikov, E.N. Evaluation of Aircraft Performance and Maneuverability by Computation of Attainable Equilibrium Sets. *J. Guid. Control Dyn.* **2008**, 31, 329–339. [[CrossRef](#)]
14. Klotz, I. Starship Lands, Then Bursts into Fireball. *Aviat. Week Space Technol.* **2021**, 183, 30.
15. Klotz, I. SpaceX Starship Prototype Passes Static Test Fire. *Aerosp. Dly. Def. Rep.* **2020**, 272, 4.
16. Palmer, C. SpaceX Starship Lands on Earth, but Manned Missions to Mars will Require More. *Engineering* **2021**, 7, 1345–1347. [[CrossRef](#)]
17. Owen, D.B. The starship. *Commun. Stat.-Simul. Comput.* **1988**, 17, 315–323. [[CrossRef](#)]
18. Klotz, I. Third Starship Prototype Lost During Cryogenic Tanking Test. *Aerosp. Dly. Def. Rep.* **2020**, 272, 2.
19. Norris, G. SpaceX Sticks Starship Landing After High-Altitude Flight Test. *Aerosp. Dly. Def. Rep.* **2021**, 276, 1–2.
20. Weiss, D. Creating Materials for the Starship. *J. Br. Interplanet. Soc. (JBIS)* **2015**, 68, 211–213.
21. Galea, P. Machine Learning and the Starship—A Match Made in Heaven. *J. Br. Interplanet. Soc. (JBIS)* **2012**, 65, 278–282.
22. Norris, G. SpaceX's Star Hopper Verifies Raptor Performance for Starship. *Aviat. Week Space Technol.* **2019**, 181, 28.
23. Klotz, I. SpaceX Starship Crashes after High-Altitude Flight Test. *Aerosp. Dly. Def. Rep.* **2020**, 274, 3.
24. Seedhouse, E. Starship. In *SpaceX*; Springer: Cham, Switzerland, 2022; pp. 171–188.
25. Klotz, I. SpaceX Prototype Starship Survives Low-Altitude Hop. *Aerosp. Dly. Def. Rep.* **2020**, 273, 3.
26. Hayes, C.; Starship Troopers. ACM SIGGRAPH 98 Conference Abstracts and Applications. 1998. p. 311. Available online: <https://dl.acm.org/doi/pdf/10.1145/280953.282447> (accessed on 10 June 2022).
27. Wang, Z.; Mao, S.; Gong, Z. Energy Efficiency Enhanced Landing Strategy for Manned eVTOLs Using L1 Adaptive Control. *Symmetry* **2021**, 13, 2125. [[CrossRef](#)]
28. Zhang, Y.J.; Zuo, G. Numerical simulation on aerodynamic characteristics of new type control surface of Starship. *Acta Aeronaut. Astronaut. Sin.* **2021**, 42, 624058. (In Chinese)
29. Parsons, D.G.; Levin, D.E.; Panteny, D.J.; Wilson, P.N.; Rask, M.R.; Morris, B.L. F-35 STOVL Performance Requirements Verification. In *The F-35 Lightning II: From Concept to Cockpit*; American Institute of Aeronautics and Astronautics: Reston, VA, USA, 2022; pp. 641–680.
30. Walker, G.; Allen, D. X-35B STOVL Flight Control Law Design and Flying Qualities. In Proceedings of the 2002 Biennial International Powered Lift 641 Conference and Exhibit, Williamsburg, VA, USA, 5–7 November 2002; pp. 1–13.
31. Osder, S.; Caldwell, D. Design and robustness issues for highly augmented helicopter controls. *J. Guid. Control Dyn.* **1992**, 15, 1375–1380. [[CrossRef](#)]
32. Carter, J.; Stoliker, P. Flying quality analysis of a JAS 39 Gripen ministick controller in an F/A-18 aircraft. In Proceedings of the AIAA Guidance, Navigation, and Control Conference and Exhibit, Dever, CO, USA, 14–17 August 2000; pp. 1–20.
33. Yang, X.; Fan, Y.; Zhu, J. Transition Flight Control of Two Vertical/Short Takeoff and Landing Aircraft. *J. Guid. Control Dyn.* **2008**, 31, 371–385.
34. Gerontakos, P.; Lee, T. Trailing-edge flap control of dynamic pitching moment. *AIAA J.* **2007**, 45, 1688–1694. [[CrossRef](#)]
35. Andrews, J.; Andrews, D. Designing reusable launch vehicles for future space markets. In Proceedings of the AIAA Space 2001 Conference and Exposition, Albuquerque, NM, USA, 28–30 August 2001; p. 4544.
36. Zhong, Y.; Liu, D.; Wang, C. Research progress of key technologies for typical reusable launcher vehicles. In *IOP Conference Series: Materials Science and Engineering*; IOP Publishing: Bristol, UK, 2018; Volume 449, p. 012008.